Aeroacoustic Study of a Strut Braced Ultra High Aspect Ratio Wing

Yuan He,[*] and David Angland.[†]
Faculty of Engineering and Physical Sciences,
University of Southampton, Southampton, SO16 7QF, United Kingdom

To enhance aerodynamic efficiency, reduce fuel consumption, and minimize emissions in the next-generation of air transport, a strut-braced Ultra-High Aspect Ratio Wing (UHARW) is a promising solution. However, the addition of a bracing strut may have aeroacoustic implications. This paper assesses the noise generated by a strut-braced UHARW, focusing on two primary source types. The first is dipole noise and the second is trailing-edge noise from both the main wing and bracing strut. Wall-Modelled Large Eddy Simulations (WMLES) and Ffowcs-Williams & Hawkings equation are used to calculate the dipole noise. The results indicate a noise increase of approximately 3.5 dB over a wide frequency range due to the bracing strut at the local spanwise section where it is located. The trailing edge noise of the main wing and strut is estimated using the trailing-edge noise prediction model of Brooks, Pope and Marcolini. The noise of a full-span, realistic UHARW wing is estimated using a model based on the time domain FWH equations and spanwise strip theory. It is found that the addition of the bracing strut increases the maximum tone-corrected Perceived Noise Level by approximately 0.8 PNLdB at the wing source level, without considering other airframe or engine noise sources.

I. Introduction

THE increasing volume of air traffic necessitates that the next generation of aircraft are more sustainable and fuel-efficient. As well as reducing fuel consumption, reducing emissions, including CO_2 and NO_x, the community noise also needs to be reduced to minimise the impact of air travel. In pursuit of these aspirations to reduce emissions,

national and multi-national programmes have investigated a range of advanced technologies to reduce the environmental impact of air travel [1, 2]. Among various approaches, the configuration of an Ultra-High Aspect Ratio Wing (UHARW) holds particular promise. Key benefits of UHARW in aircraft design include an increased lift-to-drag ratio, reduced induced drag, and enhanced fuel efficiency. However, a notable drawback of the UHARW configuration is the potential for a large bending moment, particularly in the absence of additional structural support for the wing. This can result in a significant weight penalty, highlighting the importance of carefully addressing structural considerations in the design. To mitigate this potential wight penalty, a strut-braced wing (SBW) is employed to decrease the bending moment and consequently to reduce the weight of the wing [3]. The strut braced UHARW, aimed at enhancing aerodynamic efficiency and reducing fuel usage and emissions, has been the subject of study by several researchers [4-6].

Another challenge to the next generation of commercial aircraft is the need to minimise noise and mitigate the impact of air travel on communities. In the design and certification process of a large aircraft, the airframe noise is important. Among the noise sources associated with the airframe, high lift devices on the wing and landing gears are the two most significant sources of airframe noise. Airframe noise is especially important in the approach to landing phase where it may dominate over engine noise. Even though the addition of a bracing strut enables the design of ultra high aspect ratio wings with improved aerodynamic performance, it potentially impacts noise emissions and, thus, requires careful assessment.

The addition of a bracing strut results in four potential noise sources. These are the junction of the bracing strut with the fuselage, the junction of the strut with the wing, the impact of the strut wake on the high-lift device noise, and finally the trailing edge noise of the strut itself. The first source (the junction of the bracing strut to the fuselage) is not investigated in this work. In the case where the fuselage fairing is aerodynamically well designed, the other sources will dominate over this source in the approach to landing phase.

The next two sources (the junction of the bracing strut with the wing and the impact of the bracing strut wake on the high-lift device noise) are estimated using time resolved wall modelled LES (WMLES) simulations. During the approach to landing, trailing-edge flaps are deployed to enhance the lift coefficient produced by the wing, enabling a reasonable landing speed. The outboard side-edge of a deployed trailing-edge flap generates a strong vortex due to the difference in loading between the pressure and suction surfaces of the flap. The strong flap side-edge vortex has been identified as one of the significant airframe noise sources in numerous studies dating back to the 1970s [7-10].

Slat noise dominates flap side-edge noise at low frequencies [11]. However, the noise of flap side-edge was dominant in the middle frequency range. At mid frequencies and particularly upstream, the noise generated by the outboard flap side-edge contributes significantly to the overall airframe noise. The wake generated by the bracing strut and its junction with the wing will change the flap sources and cause new acoustic sources due to the interaction of the bracing strut wake with the flaps.

The final source is the trailing-edge noise of the strut. As discussed above, the simulations were performed using a wall modelled LES approach. This was done in order to reduce the mesh size and to keep the computational cost reasonable at these Reynolds numbers. In the WMLES approach, the turbulence in the inner part of the boundary layer is modelled, removing the need to explicitly resolve it [12]. Only the turbulence in the outer boundary layer is resolved. The trailing-edge noise is caused by the scattering of pressure fluctuations due to turbulence in the boundary layer by the sharp trailing-edge [13]. Initial simulations attempted to see if the boundary layer resolution was sufficient to explicitly resolve the relevant turbulent scales responsible for trailing-edge noise. These initial simulations under-predicted the trailing-edge noise significantly (~8 dB) due to the boundary layer resolution being insufficient to capture all of the relevant turbulent scales. Since it is not possible, with the combination of the span of the bracing strut and the Reynolds number, to increase the boundary layer resolution further with the computational resources available, the trailing-edge noise will be estimated using the method of Brooks, Pope, and Marcolini (BPM) [12]. The limitations of this approach will be discussed later.

The sources, detailed above, are additional noise sources on a strut braced UHARW, in its approach to landing phase, that do not exist for conventional aircraft and are therefore important to quantify. This is the aim of this current work. In the configurations examined in this work, only the trailing-edge flaps are considered. Since the leading-edge devices would be upstream of the bracing strut, their influence on the airframe noise source due to the bracing strut is assumed to be negligible and the main effect is the interaction of the bracing strut with the wing and trailing-edge flaps.

The methodology used to determine the impact of adding a bracing strut to a high-lift wing is to perform time resolved WMLES simulations to calculate the time dependent flow field. The flow field from the computational fluid dynamics (CFD) is coupled to a Ffowcs-Williams and Hawking (FW-H) solver to determine the far field noise generated by the configuration. This methodology is validated by comparing the results to a three-element 30P30N wing. In order to predict the changes in noise sources on the full wing with trailing-edge flaps, a model based on the

time-domain FWH equations and spanwise strip theory is proposed, which uses the WMLES results in order to estimate the changes in source strength of the entire wing. This method accounts for the effect of the positions of different spanwise strips and their area changes on the overall wing noise, rather than relying on simple scaling laws. As mentioned above, the trailing-edge noise is estimated using the BPM method. The overall noise of the UHARW with a realistic geometry is estimated by combining the CFD results and the trailing-edge noise prediction results. Based on the acoustic model of a realistic wing, the changes in the noise certification values at a wing source level are calculated.

II. Methodology

A. Weakly compressible solver

A weakly compressible solver is utilized in this work. The following equations, which is derived by Inagaki et al. [14], take the compressibility into consideration at very low Mach numbers without a significant heat source,

$$\frac{1}{\rho c_0^2}\left[\frac{\partial p}{\partial t} + U_j \frac{\partial p}{\partial x_j}\right] + \frac{\partial U_j}{\partial x_j} = 0, \tag{1}$$

$$\frac{\partial U_i}{\partial t} + U_j \frac{\partial U_i}{\partial x_j} = -\frac{1}{\rho}\frac{\partial p}{\partial x_i} + \frac{\partial}{\partial x_j}\left[\frac{1}{\nu}\left(\frac{\partial U_i}{\partial x_j} + \frac{\partial U_j}{\partial x_i}\right)\right]. \tag{2}$$

Three assumptions were made for the derivation. The first assumption is that the ratio between density perturbation and mean density $\rho'/\rho \rightarrow 0$, which enables $1/(1 + \rho'/\rho) \rightarrow 1$. The second one is that the entropy is constant so that the relationship between the pressure perturbation p' and density perturbation ρ' can be expressed as $c_0^2 (D\rho'/Dt) = Dp'/Dt$. The third one is in low Mach number flows, the impact of normal stress terms is significantly smaller when compared to shear stress term. Eq.(**1**) is the new continuity equation and it is now a transport equation for pressure p. The velocity divergence serves as a source or sink term for the pressure.

The weakly compressible equations (Eqs.(**1**) and (**2**)) are solved using a modified PISO (Pressure Implicit with Split Operator) algorithm, where the coupling between momentum and pressure is adjusted. The momentum equation (Eq.(2)) can be discretised and rewritten as,

$$[A]U_j + [H] = -\frac{1}{\rho}\frac{\partial p}{\partial x_j}, \tag{3}$$

where $[A]$ is the diagonal matrix of the coefficient array and $[H]$ represent the off-diagonal matrix. Therefore, the discretised form of the velocity divergence can be written as,

$$\frac{\partial U_j}{\partial x_j} = -\left[\frac{1}{\rho}\frac{\partial}{\partial x_j} [A]^{-1} \frac{\partial p}{\partial x_j} + \frac{\partial}{\partial x_j} [A]^{-1}[H]\right]. \tag{4}$$

Substituting the continuity equation (Eq.(1)) into equation (Eq.(4)) the modified pressure equation can be expressed as,

$$\frac{1}{\rho c_0^2}\left(\frac{\partial p}{\partial t} + U_j \frac{\partial p}{\partial x_j}\right) = \frac{1}{\rho}\frac{\partial}{\partial x_j}[A]^{-1}\frac{\partial p}{\partial x_j} + \frac{\partial}{\partial x_j}[A]^{-1}[H]. \tag{5}$$

In the weakly compressible solver, the momentum equation (Eq.((2)) is incompressible. However, after the modification to account for weak compressibility, the Poisson pressure equation in the PISO algorithm [15] incorporates the time derivative and convection of pressure. When the fluid is compressible and the sound speed c_0 is considered infinite, the modified original Poisson equation for the weakly compressible solver reverts to the original Poisson equation.

B. Large eddy simulation

LES has been widely used in aerodynamic noise simulations. However, it requires a large number of cells to resolve the relevant flow structures, especially at high Reynolds numbers, resulting in a significant computational cost. For traditional wall-resolved LES, the viscous sub-layer is required to be fully resolved in all three dimensions to account for the momentum transport close to the wall. The local mesh size should be less than unity in wall units in the wall normal direction. It is not unusual for there to be some relaxation in the other two directions. An alternative to fully resolving the boundary layer down to the viscous sub-layer, is to treat the viscous sub-layer and buffer layer with a wall function. In the wall function approach, the height of the first grid point can be much greater than that in wall resolved LES. The wall function works as a bridge to account for all of the momentum transport in the viscous sub-layer, buffer layer and lower log-layer, by reproducing the correct shear stress on the wall. The utilization of wall functions is a compromise to reduce the mesh sizes in LES simulations.

Most typical wall functions do not account for the effect of adverse pressure gradients. In airframe noise calculations with separated flows, the effect of these pressure gradients are important. In this work, a modification of the Composite Wall Function (CWF) by Afzal and Gersten [16] is used. It accounts for the effect of pressure gradients.

The wall modelled LES approach used here uses WALE (Wall-Adapting Local Eddy-viscosity) model by Nicoud and Ducros [17] instead of a simple Smagorinsky model.

$$v_t = (C_w \Delta)^2 \frac{(S_{ij}^d S_{ij}^d)^{3/2}}{(\bar{S}_{ij}\bar{S}_{ij})^{5/2} + (S_{ij}^d S_{ij}^d)^{5/4}}, \tag{6}$$

where C_w is a model constant that governs the behaviour of the eddy viscosity calculation, Δ is the sub-grid characteristic length scale, $\bar{S}_{ij}$ is the strain rate tensor, S_{ij}^d is the traceless symmetric part of the square of velocity gradient tensor and defined as,

$$S_{ij}^d = \frac{1}{2} \left(\bar{g}_{ij}^2 + \bar{g}_{ji}^2 \right) - \frac{1}{3} \delta_{ij} \bar{g}_{kk}^2. \tag{7}$$

where $\bar{g}_{ij}$ is the velocity gradient tensor and δ_{ij} is the Kronecker symbol. Since a fully turbulent boundary layer is assumed by both wall function models, the WMLES can be seen a realisation of a high-Reynolds number environment. As a result, no tripping is needed for the boundary layer.

The wall modelled LES and weakly compressible solver has been implemented in a custom version of OpenFOAM at the University of Southampton. It has been successfully validated against several aeroacoustic benchmark cases [18, 19].

C. Far field noise

Most of the airframe noise from the high-lift devices is dominated by dipole noise during the approach to landing phase of flight. The exception to this is the trailing-edge noise discussed later. The CFD will only be able to determine the dipole sources, since the boundary layer turbulence is modelled in the WMLES approach and cannot explicitly be predicted from the CFD simulations. Farassat formulation 1A is a solution for the FW-H equation in free space where the solid surfaces move at subsonic speed [20]. This hybrid approach of coupling unsteady CFD with an FWH solver has been successfully used in the prediction of noise generated by aircraft components, such as landing gears and high-lift devices. The derivation of this formula can be found in [20].

$$4\pi p_T'(\vec{x}, t) = \int_{f=0} \left[\frac{\rho_0 (\dot{U}_n + U_{\dot{n}})}{r(1 - M_r)^2} \right] dS + \int_{f=0} \left[\frac{\rho_0 U_n \{ r\dot{M}_r + a_0 (M_r - M^2) \}}{r^2 (1 - M_r)^3} \right] dS, \tag{8}$$

$$4\pi p_L'(\vec{x}, t) = \frac{1}{a_0} \int_{f=0} \left[\frac{\dot{L}_r}{r(1 - M_r)^2} \right] dS + \int_{f=0} \left[\frac{L_r - L_M}{r^2 (1 - M_r)^2} \right] dS$$
$$+ \frac{1}{a_0} \int_{f=0} \left[\frac{L_r \{ r\dot{M}_r + a_0 (M_r - M^2) \}}{r^2 (1 - M_r)^3} \right] dS, \tag{9}$$

where U is the velocity on the integral surface, r is the receiver vector, n is the surface normal vector, and M is the Mach number.

The loading source term is $L_i = P_{ij} \vec{n}_j + \rho u_i (u_n - v_n)$, where u denotes the fluid velocity and v denotes the surface velocity.

D. Trailing edge noise

Trailing-edge noise is caused by the scattering of pressure fluctuations caused by turbulence in the boundary layer. When these pressure fluctuations interact with a sharp trailing-edge, acoustic energy is generated and propagates to the farfield [21]. The intensity and frequency of this noise source depends on factors such as the turbulent boundary layer characteristics, Reynolds number, and trailing edge geometry. This phenomenon is a significant noise source in various aerodynamic applications, including aircraft wings, turbomachinery blades, and wind turbine blades, where the interaction between the turbulent boundary layer and the trailing edge plays a crucial role in overall noise emissions [13].

Brooks et al. [21] developed a semi-empirical prediction model of induced noise of airfoils encountering steady smooth flow. The prediction is based on available aerodynamic and aeroacoustic experimental data from wind tunnel tests on different chord lengths of a NACA0012 airfoil. If sufficient information is known about the turbulent boundary layer pressure field, then the TBL-TE noise prediction can be determined using measured surface pressures [22]. The boundary layer characteristics depend on Reynolds number and the angle of attack. Brooks et al. [21, 23, 24] developed equations for calculating the boundary layer characteristics (thickness, displacement thickness and momentum thickness) for tripped and untripped airfoils, using wind tunnel experimental data.

III.   Numerical methodology

A. Geometry and mesh of the CFD model

Figure 1 illustrates the ultra-high aspect ratio wing with the bracing strut installed. The strut braced wing geometry investigated here is based on the work of Jones et al. [25]. This paper will quantify the aeroacoustics of this strut braced wing in a high-lift configuration. The wall modelled LES simulations cannot be performed on the entirety of the span of the full size high lift wing due to the large computational costs. A spanwise section is necessary to ensure the computational cost is reasonable for such a high aspect ratio wing. Therefore, three CFD simulations of the basic elements shown in Figure 2 are performed. Subsequently a model is used to estimate the aeroacoustics of the full span wing (detailed later). A baseline case, as shown in Figure 2(a), with just the spanwise section of the high-lift wing without the strut and junction. Figure 2(b) depicts the same spanwise section but with the strut and junction included. The flap side edge is also an important noise source in the high-lift configuration. As stated in the introduction, this flap side-edge vortex has been identified as a strong airframe noise source [7]. Thus, a flap side edge is extracted from the high lift wing CAD as shown in Figure 2(c). A trimmed mesh is employed to generate the computational meshes

for these three cases. The model used in the simulations is $1/4^{\text{th}}$ scale. All the results presented later have been scaled up to full-scale. The noise generated by the whole wing is then constructed using these basic elements using a model that is discussed later. The final cell numbers of three cases shown in Figure 2 are, 33×10^6 for the baseline case, 41×10^6 cells for the strut case and 16.3×10^6 cells for the flap side-edge case.
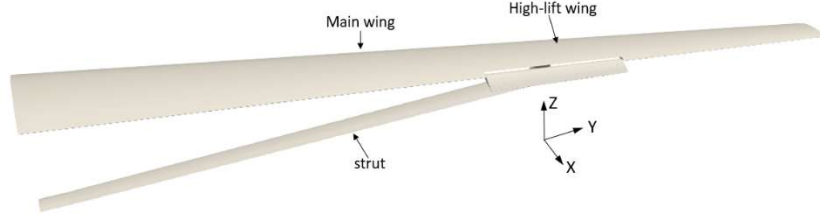
Figure 1 The strut braced ultra-high aspect ratio wing.

These simulations will quantify the additional increase in noise due to the wake of the strut and its junction interacting with the trailing-edge flap. The final part of the work is to estimate the increase in the noise due to this additional source on the whole span of a realistic wing with flaps deployed using these basic elements.
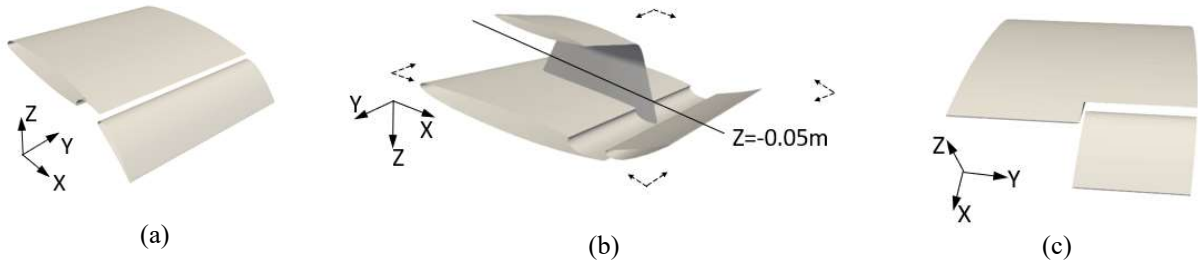

Figure 2 The basic elements of the high lift wing used in the acoustic model. (a) baseline configuration, (b) strut configuration (bottom view, the lines show the z location of the x-y plane used to show the mesh slice through the bracing strut), (c) the flap side edge.

Table 1 Surface grid parameters for the three basic element models

Configuration	$(\Delta x^+, \Delta y^+, \Delta z^+)_{av}$	$N_{x,\text{wing}}$	$N_{x,\text{flap}}$	$N_{x,strut}$	N_z
Baseline, Strut and Flap side edge case	(54, 12, 54)	1.7×10^3	0.8×10^3	0.9×10^3	1.5×10^3

Examples of the trimmed mesh are shown in Figure 3. The grid generation is performed using snappyHexMesh based on OpenFOAM v2112. The grid parameters for the three cases are listed in Table 1. A total of eleven refinement zones, including ten volume refinement zones and one zone covering the solid are implemented in the grid generation process. Figure 3 shows the different volumetric refinement zones for the three cases and the relevant cell sizes. Each refinement zone decreases the mesh size by half of the preceding one. The finest zone has a mesh size of 0.45 mm. This mesh size can resolve up to approximately 9.5 kHz (full scale) assuming 20 points per wavelength.
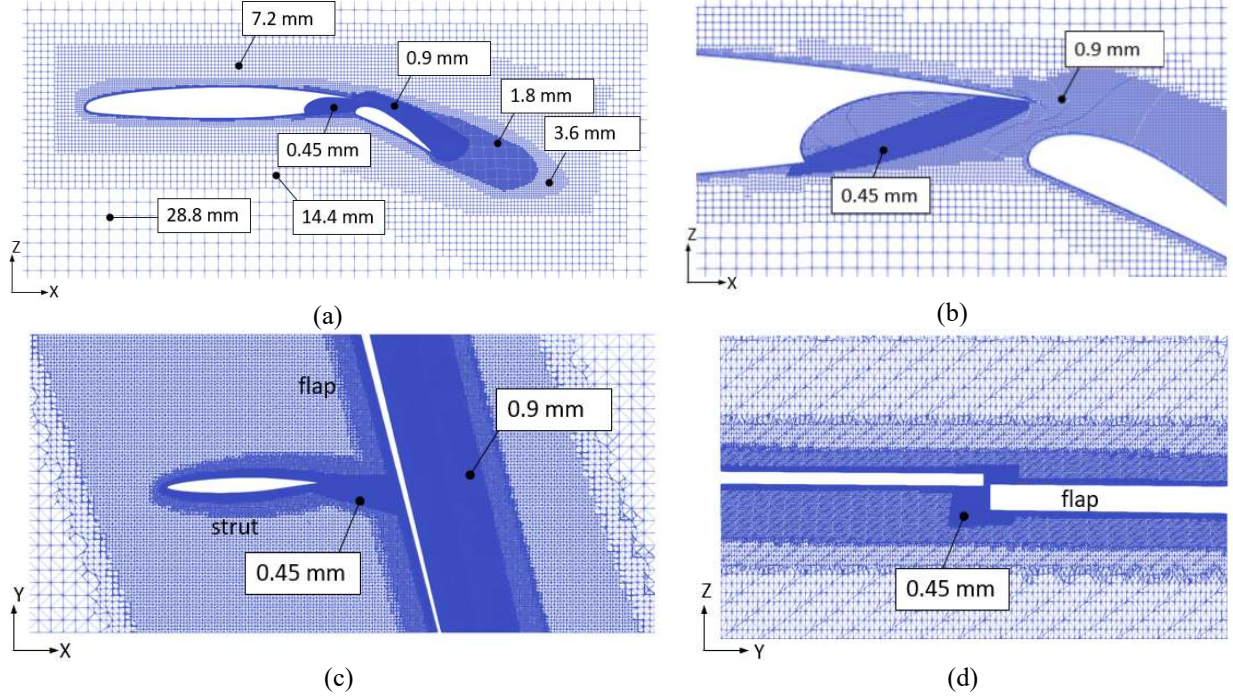
Figure 3 Mesh details. (a) baseline case at a plane normal to the spanwise direction, (b) partial enlarged view of the flap cove region, (c) partial enlarged view on *x-y* plane shown in Figure 2(b), near the bracing strut and wing junction for the strut configuration, (d) partial enlarged view of the flap side-edge region.

For the baseline case depicted in Figure 3 (b), the finest zone covers the trajectories of the shear layer within the flap cove region. In the strut case illustrated in Figure 3 (c), the finest zone not only covers the cove region, shown in Figure 3 (b), but also extends to include the wake region of the strut. In the flap side-edge case shown in Figure 3 (d), the side-edge area is also covered by the finest zone. It should be noted that, in order to reduce the computational cost, the refinement zone is not extended to the full spanwise extent. Only the spanwise positions of interest are covered and the other spanwise locations are less well resolved.

B. Numerical settings

In the CFD simulations, a coordinate system centred on the centre span of the model is employed. Within this coordinate system, the wing model remains stationary, while the oncoming flow moves in the opposite direction at the velocity of the aircraft. As seen in Figure 4 (a), the inlet plane is defined as a velocity inlet boundary condition (78 m/s) and the outlet plane is specified as a zero-pressure outlet boundary condition. The upper and lower planes are both set to zero-gradient pressure outlet boundary condition. As mentioned above, in order to reduce the computational cost, the entire full span high-lift wing will not be simulated. Instead, the simulation will focus on a

finite spanwise section centred at the mid span of the flap. Therefore, symmetry boundary conditions are applied to the front and rear planes. The wing and flap are set as non-slip walls.

In order to get the correct aerodynamic loading for these limited span WMLES simulations, the angle of attack was tuned using initial Reynolds-averaged Navier–Stokes (RANS) simulations. The procedure was to first calculate a RANS solution on the full span 3D wing including wing tip effects. The lift was integrated from this solution over the limited spanwise section that corresponded to the limited span WMLES simulations. Then the angle of attack was tuned in RANS simulations in order for the limited span simulation with symmetry boundary conditions to achieve the same sectional lift as the full 3D wing at that spanwise section. In this way, the tuned angle of attack ensured that the limited span WMLES simulations with symmetry boundary conditions still produced a realistic amount of lift corresponding to that spanwise section on the full 3D wing.
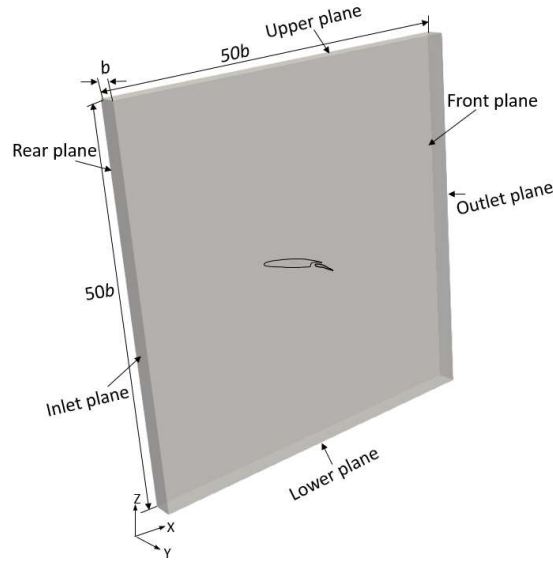

Figure 4 Boundary conditions of the simulation.

The weakly compressible solver [19] introduced in Section II is employed to obtain the unsteady flow field. To balance the simulation accuracy and computational cost, the wall modelled LES is employed, using the WALE SGS model previously described. The flow simulation is conducted by using a customised version of OpenFOAM v2112.

A second-order Total Variation Diminishing (TVD) scheme is employed to maintain computational stability and sufficient accuracy. Gauss linear is applied in the interpolation of the convection term. The "backward" time scheme, which is second order implicit, is chosen as the time stepping scheme.

In the acoustic simulation, the second order time derivative scheme is utilized. As shown in Figure 5, nineteen receivers are set in a half circle of radius 20 m around the models at intervals of 10°. The receivers are located at the mid-span of the high-lift wing.
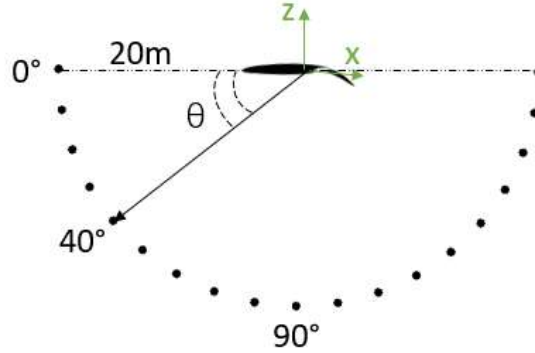

Figure 5 Receivers around the high lift wing.

IV. Benchmark validation

In this section, the grid strategy and the numerical settings will be validated through the simulation of the 30P30N three-element airfoil. As previously mentioned, the numerical methodology has previously been validated on several bluff body and landing gear benchmark cases but not on a high-lift wing. In this high-lift, strut braced wing case, the high-lift configuration is a two-element wing as the bracing strut wake only interacts with the flap. In terms of validation, the on-surface pressure distributions are compared and also the broadband levels of the noise. Tones associated with slat noise are not the focus of this current work and only the broadband noise associated with the trailing-edge flap system is of interest. The validation for the numerical methodology in this work employs the three-component 30P30N configuration. It is important to note that this configuration is an extruded 2D geometry and does not contain a flap side edge or sweep like the configuration investigated in this study. However, it still produces noise in the particular frequency ranges that are relevant even when a flap side-edge is present. Therefore, it is useful to determine the boundary layer resolution necessary to accurately capture the correct aerodynamic behaviour of this high lift configuration and the mesh resolution necessary to capture the relevant frequency range even if all the same acoustic sources are not present. The profile of the 30P30N model is illustrated in Figure 6. The stowed chord c is 0.457 m, and the slat and flap chord are 0.15c and 0.3c respectively. The deflection angle of the slat and flap relative to the main element is 30°. The slat and flap deflections are consistent with those used in the experimental study by

Pascioni and Cattafesta [26]. In order to reduce the computational cost, a spanwise length of 0.05m is selected, which is consistent with other numerical studies [27].

The grid refinement strategy discussed in section III is employed to discretize the 30P30N model. Two cases are presented to show grid convergence on both aerodynamic and acoustic results. Table 2 presents the grid parameters of the two cases. The refinement zones near the main element and the flap are similar with those applied for the baseline case, as shown previously in Figure 3 (a) and (b). Similar to the refinement in the cove region of the main element, the cove region of the slat is also refined using the grid with the second finest resolution. Additionally, the region with the slat shear layer is also refined by the finest grid. In case B, the grid parameters in the volume and boundary layer are identical to those used for the subsequent simulations on the baseline, strut and flap side-edges cases discussed in section III. The height of its first boundary layer grid in case B results in the maximum y^+ of 100 near the leading edge of the slat and an average y^+ of approximately 7. The wall functions used in this study are suitable across this range of y^+ values. A finer mesh case (Case F) was used to demonstrate grid convergence. In this case, the grid in the slat cove region is refined by halving its grid size.

The boundary conditions are consistent with those used in section III with the exception of applying periodic boundary condition to the front plane and rear plane. The inlet velocity is 58.65 m/s corresponding to a Mach number of 0.17. The attack of angle in the simulation is set at 5.5°, which corresponds approximately to 10° in the experiments conducted in the wind tunnels with Kevlar wall [26, 28].
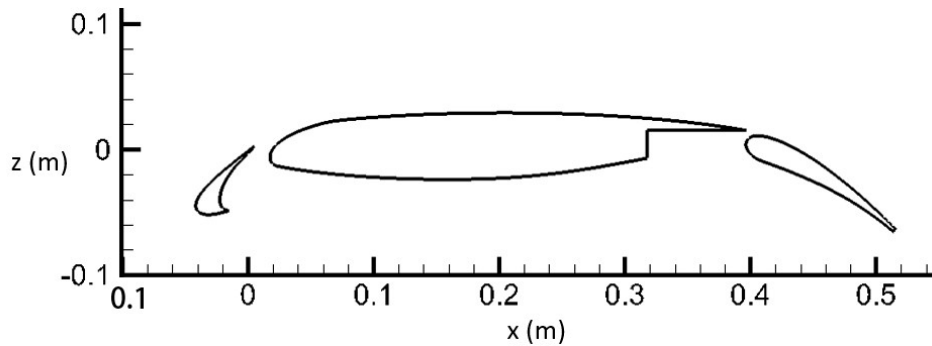

Figure 6 Profile of the 30P30N.

Table 2 Grid parameters for the simulations of 30P30N.

Case	Min grid size (mm)	Height of prism layers (mm)	Average y^+	Cells
B	0.45	1.59	7	3.8×10^6
F	0.225	0.92	8	6.5×10^6

Figure 7 shows the pressure coefficients of the simulated cases compared to the experiment conducted by Pascioni and Cattafesta [26]. For the slat, main element and flap components, case B and case F both have a good agreement with the experimental data demonstrating that the current numerical methodology is capable of capturing the correct aerodynamic behaviour.

The pressure fluctuations on the solid surfaces of case B and case F serve as input data to the Ffowcs-Williams & Hawkings solver (Eq. (9)). Figure 8 compares the one-third octave band noise spectra at a polar angle of 90°, as defined in Figure 5. Pressure monitors were positioned within the slat cove, main element cove, and along the suction surface of the flap in the spanwise direction. The spanwise coherence and spanwise correlation coefficient were both determined. The correlation coefficient decreases to values <0.25 near the midplane, which is consistent with findings by Zhang et al. [27]. This confirms that the current spanwise length is sufficient for applying periodic boundary conditions. The final spectra for case B and case F are scaled to the experimental span using the correction of Kato et al. [29].

$$
\begin{aligned}
L_c(f) &\leq L_s & \Delta\mathrm{SPL}_{\mathrm{corr}}(f) &= 10\log_{10}(L/L_s) \\
L_s &\leq L_c(f) \leq L & \Delta\mathrm{SPL}_{\mathrm{corr}}(f) &= 20\log_{10}(L_c(f)/L_s) + 10\log_{10}(L/L_c(f)) \\
L &\leq L_c(f) & \Delta\mathrm{SPL}_{\mathrm{corr}}(f) &= 20\log_{10}(L/L_s)
\end{aligned}
\tag{10}
$$

where L is the whole span length in the experiment, L_c is the equivalent coherent length, which corresponds to the spanwise spacing where the coherence is 0.5, and L_s is spanwise length in the simulation.

Both the experimental data sets presented here are from beamforming measurements, which exclude the additional noise generated by the interaction between the wing and the end plates, unlike the single microphone measurements. It can be seen that the broadband noise spectra of case B and case F are quite similar. All numerical results agree reasonably well with the data from [26] up to a frequency of 5 kHz. It is important to remember that the purpose of the current numerical setup is not to accurately resolve tones originating from the slat, but to accurately predict the broadband noise due to the trailing-edge flaps and the changes to it when the bracing strut is added and interacts with the flap system. The on-surface pressure distributions show that the current numerical setup and wall functions are accurately able to correctly capture the flow.

Based on the comparison above, the grid parameters of both case B and case F are acceptable to the simulations. However, to reduce computational costs, the grid parameters of case B are selected for the simulations in this work.
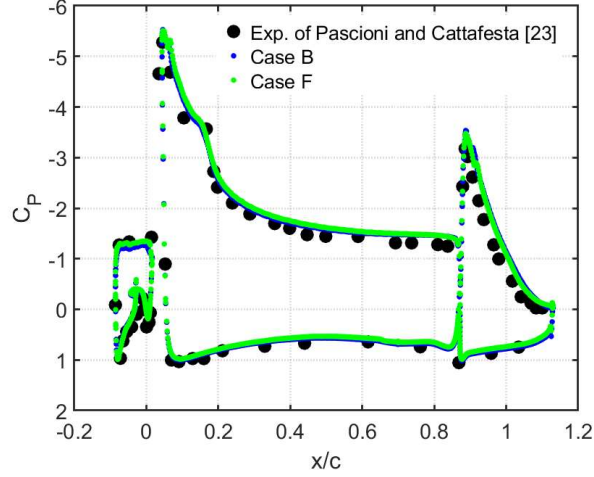
Figure 7 Pressure coefficient C_P of the 30P30N. The experimental data is from research by Pascioni and Cattafesta [26].
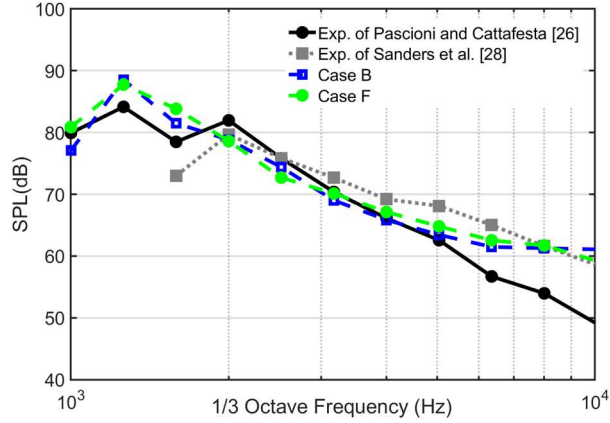

Figure 8 Comparison of noise spectra of the 30P30N. The experimental measurements are from [26] and [28].

V. Aerodynamic results

The unsteady simulations were conducted using a physical time step of 1×10^{-6} s for the baseline and strut cases, and 5×10^{-7} s for the flap side-edge case. The maximum CFL was below 0.8.

After the initial transients are discarded (first 0.7 s) the data sampling starts. Since the realistic wing model based on spanwise strip theory (presented later) will utilize data sampled from these basic element simulations (shown in Figure 2 (a)), a relatively long time signal is required so it can be divided into different time blocks that are then mapped onto different spanwise strips. The surface pressures are sampled for an additional 1.2 s. This gives a total simulation time of 1.9 s corresponding to approximately 210 flow-through times based on the high lift wing chord. The computational wall-time for this process totalled approximately 520 hours for the baseline and the flap side-edge cases, and 584 hours for the strut case, utilizing 320 processors on the Iridis5 cluster at the University of Southampton.

Figure 9 displays contours of the instantaneous vorticity on various planes. Figure 9(a) and (b) shows the vorticity of the centre span plane of the baseline case. The boundary layer on the pressure surface of the wing, separates from the wing at the cove edge and breaks down into an unsteady shear layer in the cove. The two shear layers from the suction and pressure surface merge above the suction surface of the flap. The boundary layer on the suction surface of the flap separates upstream of the trailing-edge. This separated shear layer again exhibits unsteadiness in the time resolved simulations.

Figure 9(c) presents the vorticity field at the plane perpendicular to the z direction. This plane shows the wake from the bracing strut and its interaction with the flap surface. It can be observed that an unsteady wake is generated downstream of the trailing edge of the strut and subsequently impinges on the pressure surface of the flap. Figure 9(d) shows the vorticity at the flap side-edge case at this geometry's centre span, which extends through the gap between the side edge of the flap and the wing. Compared to the baseline case shown in Figure 9(a) and (b), the flow in the cove region and near the suction surface of the flap is significantly different. This is caused by the roll up of the strong flap side-edge vortex.
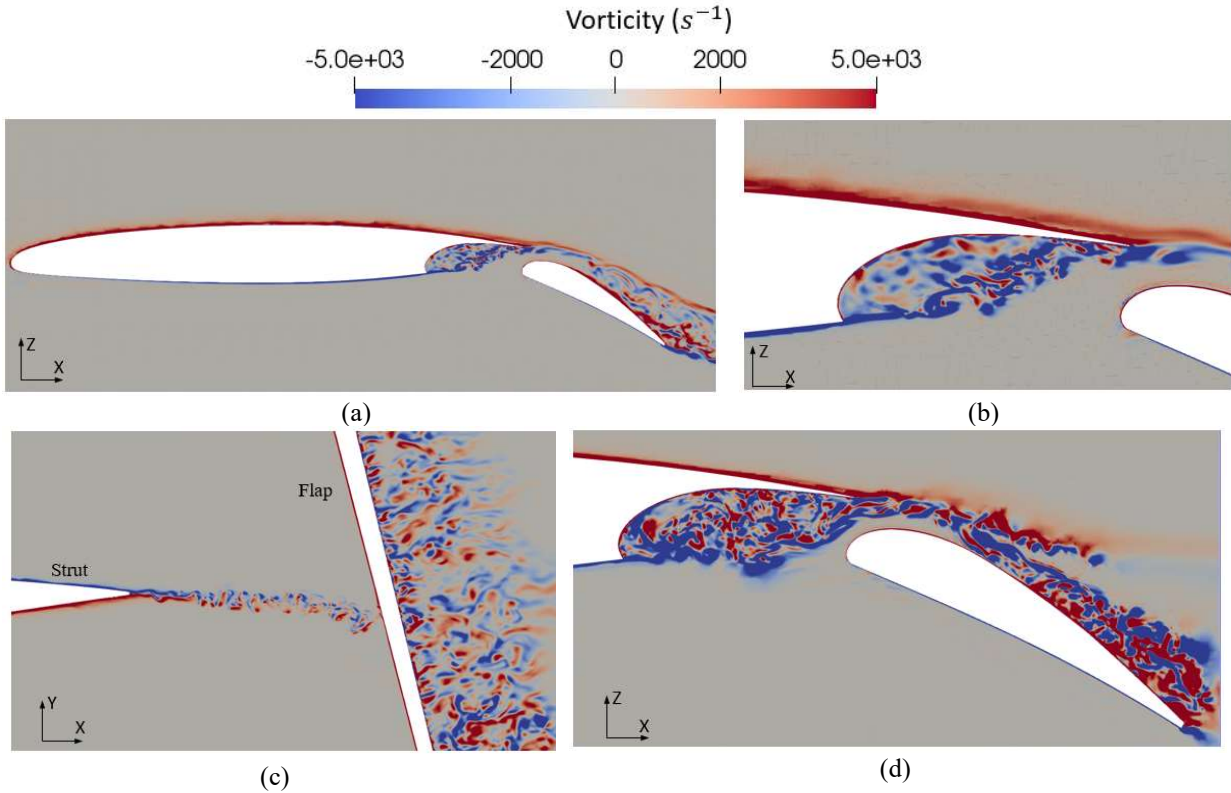

Figure 9 Contours of instantaneous vorticity. (a) y vorticity at mid-span of the baseline case, (b) y vorticity in flap cove region, (c) z vorticity at region near the bracing strut trailing-edge, (d) y vorticity at region near the flap side edge.

In order to visualize the 3D structures in the flow, the Q criterion is shown in Figure 10. As observed in Figure 10(a) and (b), the main vortical structures are located in the flap cove region and in the unsteady shear layer over the suction surface of the flap. In the strut case, shown in Figure 10(c), a significant turbulent wake is generated downstream of the trailing-edge of the strut. This wake convects downstream and impinges primarily on the pressure surface of the trailing-edge flap. This bracing strut wake interaction with the flap is an additional source of noise due to the presence of the strut in the UHARW configuration. Figure 10(d) illustrates the roll-up of the flap side-edge vortex. The flow field at the flap side-edge is dominated by two vortices that merge to form a single larger vortex. Near the leading-edge of the flap, a vortex is formed as the boundary layer separates from the pressure surface and forms a free shear layer. This vortex is the primary vortex. On the suction surface of the flap, a smaller secondary vortex forms. The vortices grow in size and strength along the chord of the flap. Eventually they merge together to form a single large vortex.
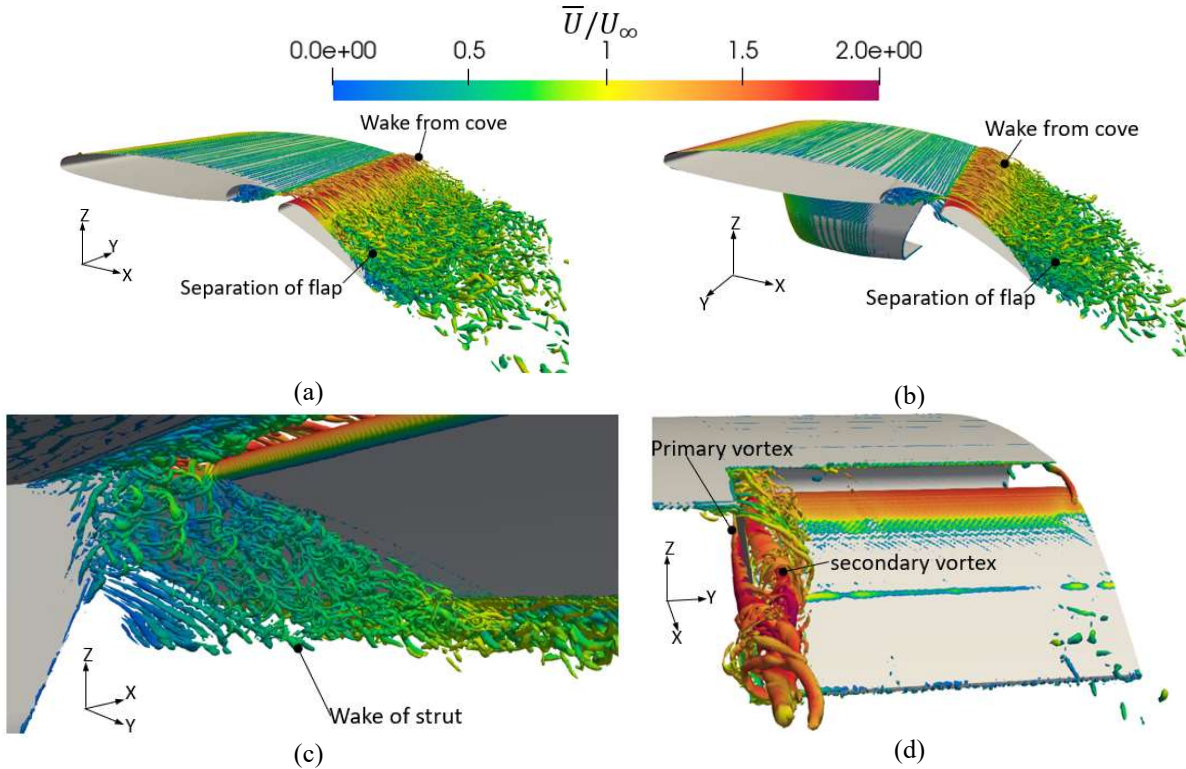

Figure 10 Iso-surfaces of instantaneous Q criterion (5×10^7 s^{-2}) coloured by the velocity ratio. (a) baseline case, (b) strut case, (c) wake region behind the bracing strut, (d) flap side edge case.

The flow field around the high-lift wing exhibits unsteady, turbulent wakes which result in unsteady pressure fluctuations on the solid surfaces of the wing and flap, which form sources of dipole noise. The ultimate source of

these unsteady pressures are the vortex shedding, flow separation and impingement of turbulent wakes [30]. In the context of far-field noise, the time rate of change of pressure, denoted as dp/dt, on the surface is a measure of the dipole source strength on the surface [31]. To locate areas with strong noise sources, Figure 11 displays the dipole source strength, integrated across the frequency ranging from 20 Hz to 2000 Hz.

$$L_{\dot{p}} = 10 \log_{10} \left(\int_{f_1}^{f_2} \text{PSD}(dp/dt) df \right), \tag{11}$$

where $\text{PSD}(dp/dt)$ is the power spectra density of the dp/dt signal (a measure of the surface dipole source strength in units of Pa^2/s^2) and f_1 and f_2 are the integral frequency limits. The reference value in the calculation of the logarithm in Eq. 11 is simply 1 Pa^2/s^2 as the plots are only used to illustrate relative dipole source strength.

Figure 11 (a), (b) and (c) display the pressure fluctuations on the surfaces of the baseline case and strut case. The suction surface of the flap and the cove surface towards the trailing-edge are significant noise sources. This is attributed to the interaction of these regions with the unsteady shear layer from the wing surfaces and the suction surface of the flap, as depicted in Figure 9 (a) and (b). As shown in Figure 11 (c), the wake of the bracing strut increases the dipole source strength on the pressure surface of the flap and the strut-wing joint area. The dipole source strength also increases within the cove region where the wake from the bracing strut impinges on these surfaces. The cause of this is clearly illustrated in Figure 9 (c) where the unsteady wake generated by the strut is shown. This unsteady wake causes dipole sources on the cove and flap pressure surfaces where this wake convects close to these surfaces. It should be noted that this effect is quite localised to the regions directly downstream of the bracing strut.

Figure 11 (d) depicts the dipole source strength around the flap side edge and the side edge of the cove in the main element. It is evident that the pressure fluctuations are strong around the flap side edge, which interacts with the flap side-edge vortex, as previously shown in Figure 9 (d).

The above discussion highlights the critical role played by the detached shear layers and wakes originating from the surfaces of main element cove, flap and strut wake. These unsteady flows generate unsteady pressures on the surface and the calculation of the dipole source strength on the surfaces shows where the acoustic sources are dominant on the surfaces. The next step is to propagate these to the farfield using an FWH solver in order to calculate the farfield noise.
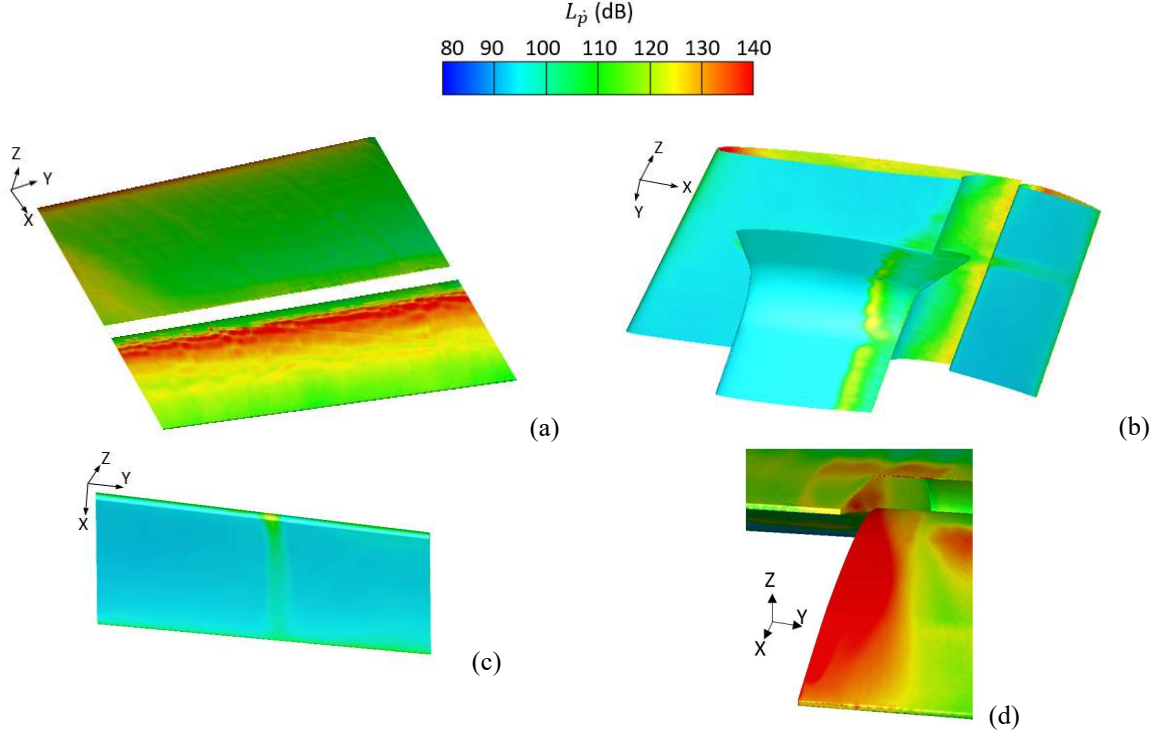
Figure 11 Contours of the time rate of pressure change, dp/dt, on the integral section of the model components surfaces. (a) suction surface of baseline case (b) pressure surface of strut case, (c) pressure surface of flap of strut case, (d) surface near the flap side edge.

VI. Aeroacoustic results

A. Dipole noise of the basic elements

The far-field acoustic pressure is computed using Formulation 1A of Farassat [20], (Eqs. (8) and (9)). In this study, the integral surfaces are the stationary, solid surfaces of the wing and strut. The integral surface normal velocity U_n, its time derivative $\dot{U}_n$ and the velocity in the direction of surface normal change rate $U_{\dot{n}}$ are all zero in equation (8) . Consequently, the thickness noise term $p'_T(\vec{x}, t)$ is zero. Therefore, only the loading noise p'_L calculated by Eq. (9) is used in the integration. It is the time-domain solution of the FW-H equations, with the time-varying pressure on the solid surfaces as an input. Figure 12 shows the A-weighted noise spectra of the three basic element simulations at the receiver of 90° (corresponding to when the aircraft is directly overhead). A-weighting is used as it attempts to account for the relative loudness perceived by the human ear.

Since the majority of the sampled pressure data was to be used for the realistic wing model based on spanwise strip theory (presented later), only a small amount of the available time signal was used in the FWH solver for the basic element simulation results (0.2 s). The PSD of the sound pressure signals is determined using Welch's method,

employing a Hanning window with a 50% overlap for each segment. The frequency bandwidth was 10 Hz. Then, these spectra are integrated into one-third octave bands after being rescaled to correspond to the full-scale aircraft assuming a constant Strouhal number for the frequency scaling and the dipole scaling law for the amplitudes [32, 33] using the equations below.

$$\Delta\text{SPL} = 10\log_{10}(S_1/S_2), \tag{12}$$

$$f_1/f_2 = (L_{C2}/L_{C1}), \tag{13}$$

where ΔSPL is the adjustment to the sound pressure level, S_1/S_2 is the reference area ratio of the model, f_1/f_2 is the frequency ratio, and L_{C2}/L_{C1} is the ratio of the characteristic length of the model. Subscript 1 represents the full-scale aircraft, and 2 corresponds to the CFD model scale (1/4th). As discussed previously, the CFD model was reduced to 1/4th scale to reduce computational cost. The freestream velocity remained unchanged. Eq. (12) is used to scale the acoustic results assuming a dipole source, and Eq. (13) is used to scale the frequency assuming a constant Strouhal number [32].

In the validation case, Eq. (12) was applied to scale the small spanwise length to match the experimental long spanwise length. In the current case, the spanwise coherence and spanwise correlations have also been determined. The scaling applied is consistent with the correction of Kato et al. [29]. The frequencies and narrowband SPLs are scaled to the values of the full-size configuration using the dipole scaling laws in Eq. (12) and (13). Subsequently, the full-scale noise spectra are converted to A-weighted by applying the A-weighting curve. It should be noted that although the signal length is only a relatively small amount of the data available, the small number of block averaging in the FFT calculation has only a small influence on the one-third octave band data presented here. This has been assessed.

It can be observed in Figure 12 that the A-weighted Sound Pressure Levels (SPLs) of the noise spectrum of the strut case is greater at almost all frequencies than that of the baseline case without the bracing strut. This difference is primarily caused by the influence of the wake generated by the bracing strut and its joint to the wing. Figure 11 (b) and (c) provide a clear illustration of the on-surface dipole source strength showing this phenomenon.

Compared to the noise spectra of the baseline case and the strut case, the noise spectrum generated by the flap side edge exhibits different frequency characteristics. It produces more noise at frequencies between 300 and 1400 Hz where the flap side-edge noise dominates, while considerably less noise at lower and higher frequencies. Outside of these frequencies, the rest of the flap and wing system dominates the broadband noise.

This findings is consistent with a 1/11th scale test conducted on an A320 model [11]. It was concluded that at low frequencies slat noise dominated over flap side-edge noise. However, the noise of flap side-edge was dominant in the middle frequency range. At mid frequencies and particularly upstream, the noise generated by the outboard flap side-edge contributes significantly to the overall airframe noise.
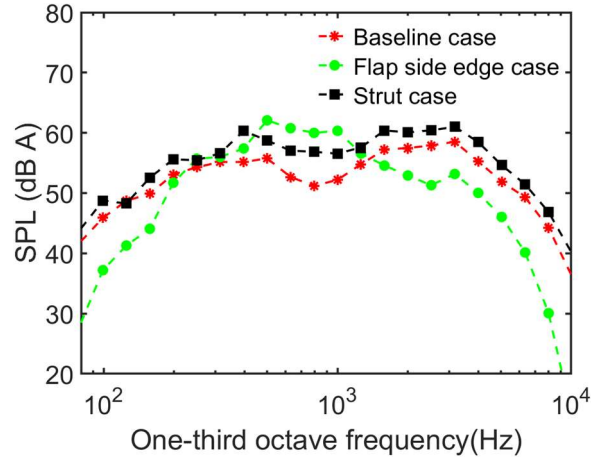

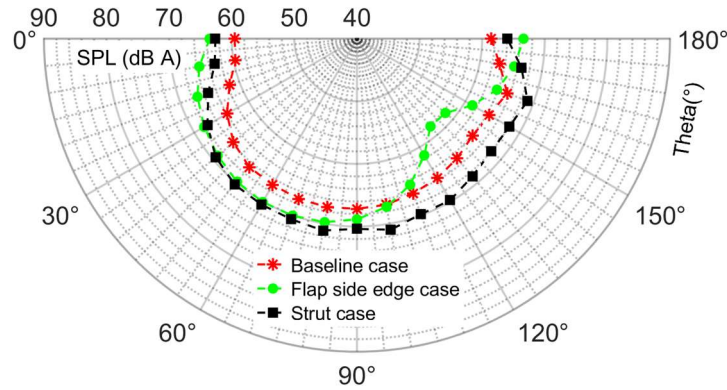**Figure 12 A-weighted noise spectra of the basic element simulations at 90°.**

Figure 13 A weighted directivity of the three simulations of the basic elements.

Figure 13 displays the A-weighted OASPLs of the three simulations at the 19 receivers in Figure 5. The strut case exhibits similar directivity to the baseline case but generates higher noise levels than the baseline case does, with an approximately 3.5 dB increase at all receivers. This difference can be attributed to the strut joint and its wake interacting with the pressure surface of the wing and the flap. Meanwhile, the noise generated by the flap side-edge case is greater at upstream and reduces in the downstream direction compared with the baseline case. The addition of the bracing strut causes a measurable increase in noise locally across the entire frequency range. However, these simulations were conducted over a very limited span. While locally there is a significant increase of up to 3.5 dB due to the bracing strut, the next thing to determine whether or not that is significant at the whole wing source level for a realistic span model with flaps.

20

B. Dipole noise of a realistic model

Figure 14 displays a realistic high-lift wing model. The spanwise length is approximately 29 m. The trailing-edge flaps occupy a realistic spanwise extent of the wing. The noise generated by this realistic wing can be divided into two parts; the trailing edge noise and the dipole noise determined from the simulations. The trailing edge noise is determined for the main wing and the strut (if the strut is installed). The dipole noise is mainly generated by the two-element high-lift wing, flap side edge between the high-lift and main wing, and the bracing strut joint with the wing, as shown in Figure 2(b). The estimation of the trailing edge noise will be discussed in the next section. As for the dipole noise, it is very computational expensive to be directly calculated by CFD due to the high aspect ratio. Therefore, the numerical results of the basic elements, as shown in Figure 2 and presented in the previous section, are used to estimate the dipole noise of the whole high-lift part of the full-sized realistic wing.
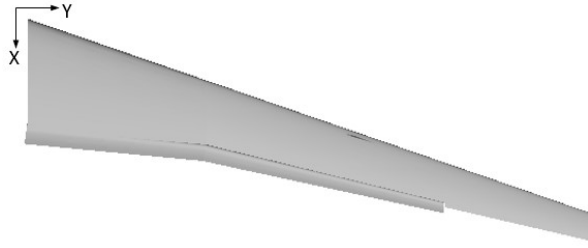

Figure 14 Realistic two-element wing model.

To calculate the noise of this model, the entire high-lift part of the realistic wing is divided into 12 spanwise segments or strips as shown in Figure 14. Each strip has the same spanwise length. The baseline case and strut case, as shown in Figure 2(a) and (b), are located at the position of segment 2. The time history of surface pressures of the baseline case (segment 2) has been collected for approximately 1.2 s. The acoustic signals of these blocks are assumed having the same Strouhal number and the differences of the amplitude are only produced by the differences of the segments area. This is clearly an approximation. Due to the effect of sweep, taper etc., there will be differences in the flow and acoustic sources along the span. These are neglected in this simple model. The purpose of it is, as a first estimate, to see if the changes seen in the local source are significant on the whole wing source level.

The time resolved on-surface pressure data of the baseline case (1.2 s) is divided into 12 time blocks. Each time block has a source data duration of 0.2 s with 50% overlap with its adjacent one. Subsequently, the 12 pieces of source data are mapped to different spanwise strips of the high-lift wing, which has considered the area differences between each strip. To prevent continuous two pieces source data from being assigned to neighbouring segments, a randomised assignment is used as shown in Figure 14. The time scale of the pressure data of each segment is scaled according to

its chord length assuming that the Strouhal number is constant. Again, this is clearly an approximation. The area scaled pressures are then interpolated onto the FWH solid integration surface shown in Figure 14. The receivers, as shown in Figure 5, are placed at a position corresponding to the centreline of the fuselage. Using the time domain FWH solver (Eq.(9)), the total noise signal from all the spanwise strips is obtained considering the retarded time differences. The effect of block randomisation and signal duration on the predicted results is examined in Appendix A in order to show the sensitivity of the results to these parameters. The differences are small and only occur at low frequencies and are not significant in the A-weighted and the Perceived Noise Level (PNL) results presented in this analysis.
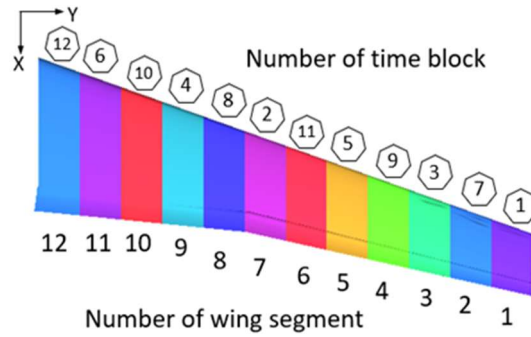
Figure 15 High-lift wing of the realistic model with 12 spanwise segments.

Compared to directly calculating the noise by simple scaling laws, the current time-domain FWH method considers the effect from the area differences between the 12 spanwise strips, as shown in Figure 14. Figure 16 depicts the acoustic results of the high-lift part of the realistic wing, as shown in Figure 14, calculated by the scaling laws and the current time-domain FWH model. When calculating the noise spectra using the simple scaling laws, the amplitude is increased by approximately 24.5 dB at every frequency, given by Eq. (12), because the area ratio is approximately 280 times of that of the baseline case that was simulated in CFD. The narrowband is then corrected assuming Strouhal number is a constant and the resultant spectrum is converted into one-third octave bands to allow the broadband signals to be compared.

Figure 16(a) shows that the noise spectra are similar at frequencies lower than 200 Hz, while there is approximately 4 dB difference at frequencies between 200 to 500 Hz and 1500 Hz to 10 kHz. In the directivity, as shown in Figure 16 (b), the noise levels of the scaling law are around 2 dB greater than those of current time domain FWH method from 50° to 180° due to not considering any coherency between the different spanwise strips. These results illustrate that the current time-domain FWH method has considered more of the effects from the variations in area along the span by using strip theory. By also considering variations in the time scale depending on the local length scale, it

results in a different prediction to simply using dipole scaling laws. As discussed above, it still contains a large amount of assumptions about the nature of the sources (constant Strouhal number etc.) across the entire wing, which are not correct for the real wing. However, the purpose of this time domain FWH model is to provide a first estimate of whether or not, the additional acoustic sources due to the bracing strut are significant at the wing source level.
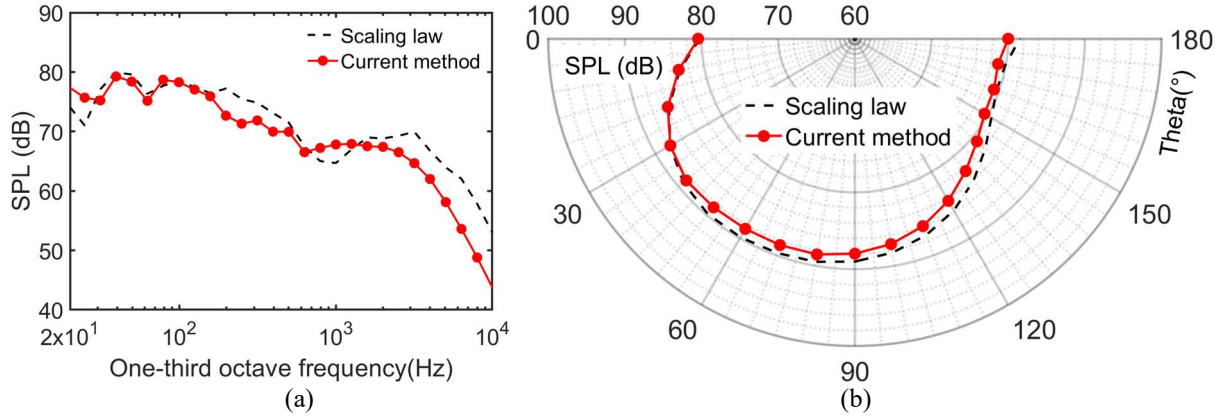

Figure 16 Noise of the high-lift part of the realistic wing. (a) One third octave noise spectra at 90°, (b) fly over directivity.

When calculating the whole dipole noise of the realistic wing with the baseline configuration, the flap side-edge case, as shown in Figure 2(c), is superimposed with the other 12 segments at the relevant spanwise strip, as shown in Figure 14. Figure 17 presents the comparison of the cumulative A-weighted noise of the baseline configuration with and without flap side-edge noise. The curves illustrate the total A-weighted noise variation as different numbers of spanwise strips are included in the model. Due to the large span of the high-lift devices in this UHARW configuration, the effect of flap side-edge noise gradually diminishes as more of the span of the trailing edge flaps is included.

In the calculation of the strut configuration, the source data of segment 2 is replaced by the one of the strut case shown in Figure 2 (b). Figure 18 depicts the A-weighted noise spectra of the realistic wing with baseline and strut configurations. It can be observed that the difference is quite small when the whole wing including the flap side edge is considered. This is attributed to the fact while the noise due to the interaction of the wake from the bracing strut on the flap was significant locally, once a realistic span flap and flap side edge sources were included, its relative contribution to the high-lift noise was small. A similar conclusion is seen in the A-weighted directivity, as shown in Figure 19. The wake from the bracing strut impinging on the flap was a relatively small source once the entire high lift wing noise was accounted for as it was dominated by other sources.
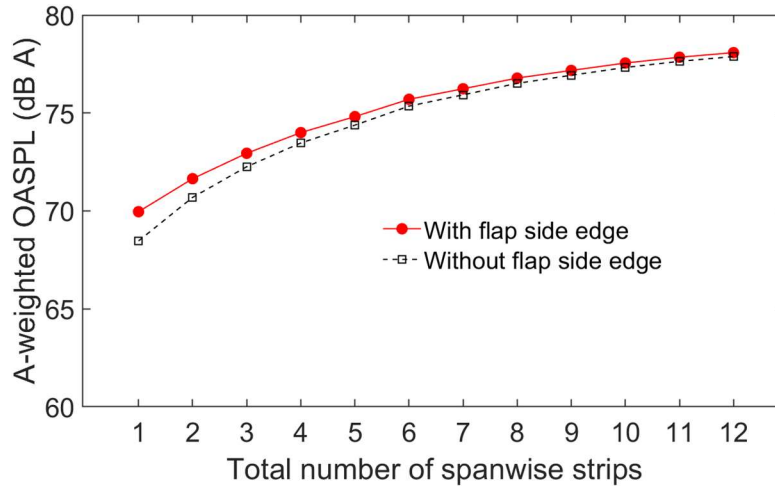
Figure 17 Comparison of A-weighted noise of the baseline configuration with and without flap side-edge noise.
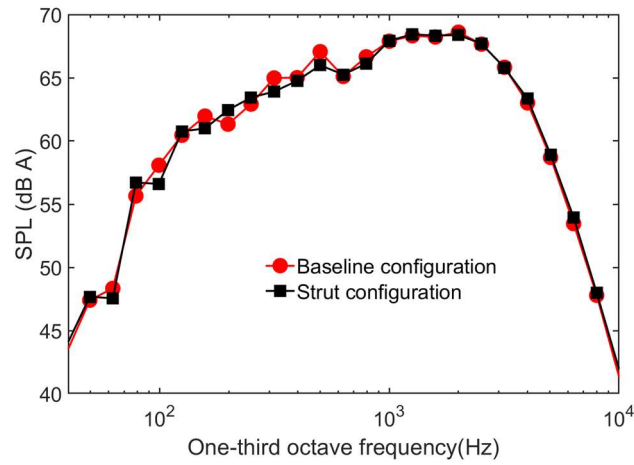

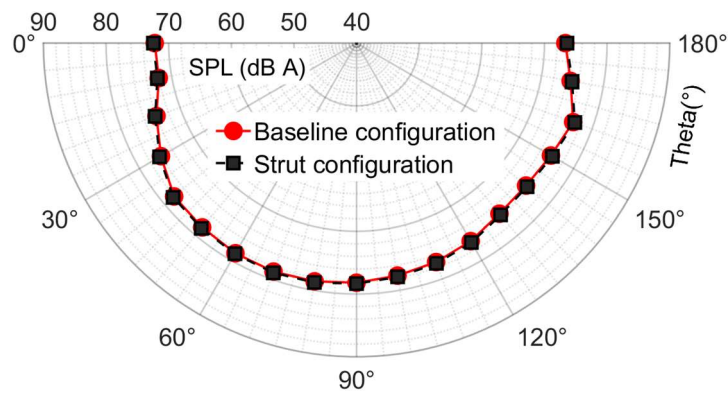**Figure 18 A-weighted noise spectra of the realistic high-lift wing simulations at 90°.**

Figure 19 A-weighted directivity of the realistic high-lift wing.
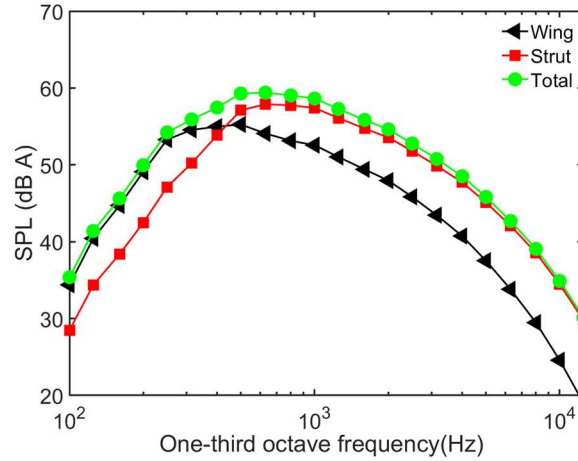
C. Trailing edge noise

Figure 20 Trailing edge noise estimated by the BPM method at a polar angle of 90° (aircraft overhead).

The relevant turbulent scales responsible for the trailing edge noise, generated by the main wing and strut, are not fully resolved in these simulations due to the boundary layer resolution, which necessitated the use of a wall modelled LES approach. This approach was chosen to keep the computational cost reasonable for these cases at these Reynolds numbers. Since not all of the turbulence responsible for the generation of trailing-edge noise is resolved, the trailing-edge noise cannot directly be determined from the numerical simulations. In order to estimate the magnitude of this additional noise source, the Brooks, Pope, and Marcolini (BPM) method is used [13]. Although this prediction method is used in many applications, it still has a number of assumptions and limitations. The tuning procedure is based on measurements of a NACA0012 airfoil. Also, the trailing-edge noise is assumed to be a function of the boundary layer displacement thickness and the angle of attack dependency for that specific airfoil [21]. The BPM method also has a tendency to over-predict high-frequency noise and cannot always accurately model the noise from blunt trailing edges [34]. In spite of these limitations, it is significantly faster than CFD-based trailing-edge noise prediction, particularly for the current model, which involves high Reynolds numbers and very high aspect ratios. The BPM method is used in this work in order to provide a first estimate of whether or not, the additional acoustic source due to the strut trailing-edge noise, is a significant source relative to the other airframe sources explicitly resolved in the numerical simulations.

The trailing edge of the deployed flap is not included in the BPM method. The original motivation for using the BPM method on the wing and strut trailing-edges, was that the turbulence responsible for the trailing-edge noise source was not explicitly resolved in this wall modelled approach, therefore necessitating the use of the BPM method to estimate it. Since the flow is separated on the suction surface of the flap, there is no attached boundary layer that convects past the sharp trailing-edge. As shown in Figure 9, the resolved shear layer from the flap cove convects over

the suction surface of the wing. Also, the turbulence in the separation region is explicitly resolved and therefore the noise can be determined from the CFD without having to resort to the BPM method to estimate sources that are not explicitly resolved in the simulation.

Since the trailing edge noise is dependent on the state of the boundary layer, calculating the boundary layer properties of the strut and main wing is essential for predicting the trailing edge noise with the BPM model. As shown in Figure 2, the WMLES computations were only performed on limited spanwise extents of the full span geometry. Performing a WMLES over the entire span would be prohibitively computationally expensive. Therefore, RANS simulations of the strut and wing profiles were performed in order to compute the boundary layer properties, which serve as an input to the BPM method. Only the boundary layer properties of the profiles with maximum and minimum chord lengths were simulated. The boundary layer properties at intermediate spanwise locations were simply interpolated between these two values. Figure 20 illustrates the noise spectra of the wing, the strut, and their sum. The full-scale noise spectra are A-weighted. For the trailing edge noise calculation of the wing, the net noise is determined by not including the contribution from flap trailing-edge since the flow is separated upstream of the trailing edge. It can be observed that the spectrum of wing is primarily dominated by low frequency noise, while the spectrum of the strut case is comparable between high and low frequencies. The green line in Figure 20 is the total noise spectrum. It is evident that the noise at frequencies lower than 600 Hz is primarily contributed by the wing trailing edge, while the strut trailing edge noise contributes more at frequencies greater than 600 Hz.

D. The whole noise of a realistic two-element wing

The total noise of the whole wing is estimated by incoherently summing the dipole noise of high-lift wing from CFD, calculated in section VI B, with the trailing edge noise, computed in section VI C. Figure 21 depicts the total noise of the baseline and strut configurations at receiver of 90°. The noise spectra are quite similar with those in Figure 18. However, there are some small differences at certain frequencies. The noise spectrum of strut configuration is approximately 1 dB greater than that of the baseline configuration at frequencies between 400 and 1500 Hz. However, at very low and high frequencies the difference is negligible. This indicates that the trailing edge noise from the strut has a small influence on the overall noise. However, it is important to note that while both dipole sources and the trailing-edge noise of the bracing strut are small when a realistic span wing is considered, the increase in noise with the bracing strut installed is still measurable.
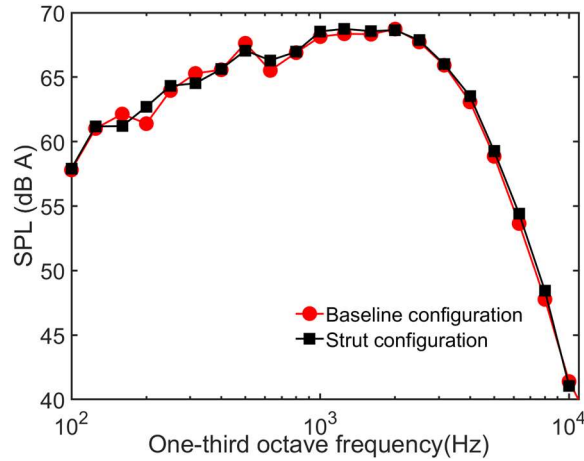
Figure 21 The whole noise spectra comparison between the baseline configuration and strut configuration including trailing-edge noise.

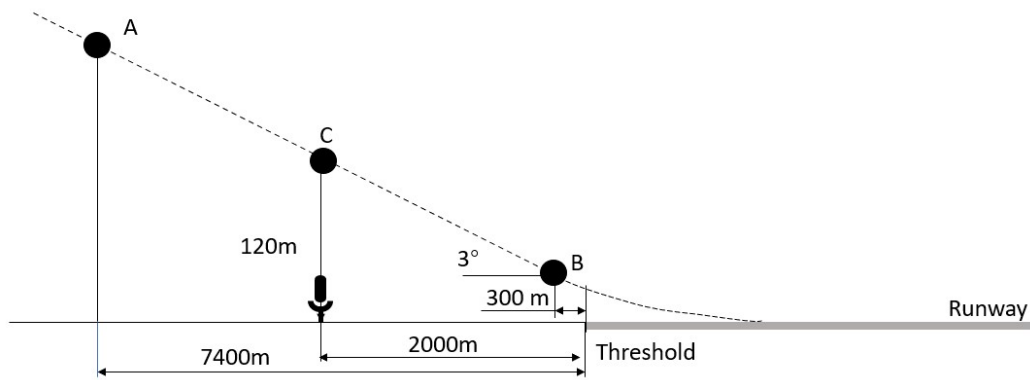## VII. Impact on Tone Corrected Perceived Noise Levels

Figure 22 Typical approach trajectory for noise certification [35].

To estimate the influence on certification levels of an approach to landing flight, the realistic ultra-high aspect ratio wing model illustrated in Figure 14 is utilized. The EPNL calculation involves analysing noise levels in the frequency domain over a fixed time interval on a reference trajectory, converting them to perceived loudness, correcting for the presence of tones and applying a duration correction. The various steps required to calculate EPNL with detailed calculation procedures are available in the relevant ICAO standard [35]. For this wing model, it is not possible to perform the whole EPNL calculation since the noise levels for the wing alone do not allow the duration correction to be properly calculated. However, the preceding steps can be calculated to give an indication of the changes in certification values.

The first step involves measuring the noise levels on an approach trajectory, as depicted in Figure 22. A Doppler shift is applied to account for the frequency shift due to relative motion of the aircraft and the observer. In the current calculation, only the high-lift wing is considered. The other airframe noise sources are not. The noise levels are calculated at various positions to mimic the trajectory used in certification. After obtaining the noise levels at the different relative receiver positions, they are converted to perceived noise levels using a noy table [35].

To adjust for the presence of tones in each spectrum, a tone correction factor C is calculated and added to PNL, resulting in tone corrected PNLT, as shown in Figure 23. The difference in the maximum PNLT between the baseline and strut case is approximately 0.8 PNLdB due to the installation of strut. However, it is important to note that this is only at two-element wing source level considered without slats, landing gear and engine sources. The actual value on an aircraft will depend on the relative magnitude of the other sources and these are aircraft specific and will change the relative importance in the change of the high-lift wing source with the addition of a bracing strut.
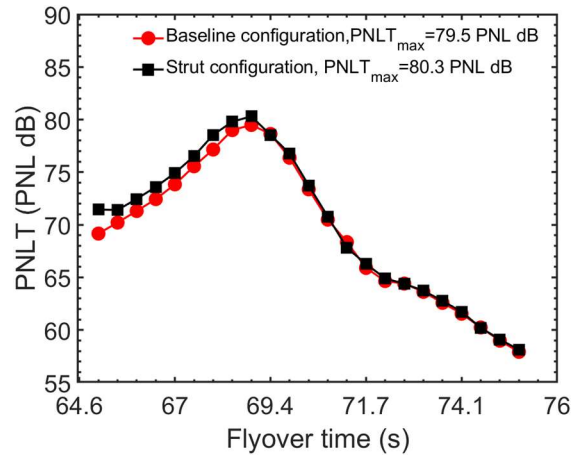

Figure 23 Perceived noise level corrected for tones as a function of aircraft flyover time.

VIII. Conclusions

An aeroacoustic study of a strut-braced Ultra-High Aspect Ratio Wing was performed. The aim is to quantify the additional increase in airframe noise due to the addition of a bracing strut and to understand its noise generation mechanism. The potential airframe noise sources were the junction of the strut with the wing, the interaction of the strut wake with the trailing-edge flaps and the trailing edge noise of the strut. The first two sources were determined using a wall-modelled LES approach, with a weakly compressible solver, to calculate the flow field around the wing. The far field acoustics were determined from this flow field using the acoustic analogy. The last source was estimated using the BPM method for trailing-edge noise. These individual sources were combined to estimate the aeroacoustic

impact of adding a bracing strut on a realistic span wing, including a representative flap and flap side edge, in order to measure the impact at aircraft wing source level.

In the flow field simulations, the flow phenomena responsible for the unsteady pressures on the surfaces were determined. These were the detached shear layer from the flap cove region, the separated flow on the suction surface of flap towards the trailing-edge, the bracing strut wake, and flap side-edge vortex. The areas affected by these unsteady flows generated strong dipole noise sources. The results shows that when the bracing strut was installed, the A-weighted noise was increased by approximately 3.5 dB over a wide frequency range on that local spanwise strip. This was due to the interaction of the bracing strut wake impinging on the flap surface. This caused a broadband source on the pressure surface of the flap and within the flap cove.

In the calculation of the trailing edge noise, it was observed that the trailing edge noise of main wing contributed more at low frequencies, while the bracing strut contributed more at high frequencies. The addition of a bracing strut introduced additional trailing-edge noise as expected.

The noise of the full-span, two-element, high-lift wing was estimated by combining the noise generated by the simulations of the basic elements to produce a model of the full span high-lift wing. The basis of this model was the time domain FWH equations using spanwise strip theory. The time data was scaled according to the local length scale and the pressure signals were interpolated onto the full-span wing in order to account for the area effects. Subsequently, the overall noise of the wing was determined by combining this noise from the time domain FWH model of a realistic full span wing and the trailing edge noise. The conclusion was that the addition of the bracing strut resulted in only a very small increase in the noise at the wing source level, as other sources dominated it such as the existing flap noise.

Based on the acoustic model of the realistic full-span high-lift wing, the maximum value of PNLT at the wing source level increased by approximate 0.8 PNLdB due to the installation of the bracing strut. It is important to note, this is only at the wing source level and does not consider the other noise sources, which will be aircraft specific. Another caveat is that no leading-edge devices are included. Depending on the detailed design of the high-lift devices, it may be possible for the slat noise to dominate especially at low frequencies. This may further reduce the impact of the additional noise due to the bracing strut on the airframe noise.

While the conclusion from this aeroacoustic study was that the wake from the bracing strut impinging on the flap was not a significant source at the whole wing level, it was still a source, and its mechanism was identified. An

unsteady wake was generated downstream of the bracing strut that impinged on the flap pressure surface resulting in a dipole noise source. Also, the trailing-edge noise of the bracing strut was still small but measurable at the whole wing level. Airframe manufacturers and designers still need to be aware of this. While in this simple configuration, it was not a significant contribution on its own, in a detailed high-lift device design it may become significant. A possible example is if this wake interacted with the flap tracks or other detailed geometries in a real high-lift system. This may increase the efficiency of this source above what was concluded in this study on a very simple configuration.

Acknowledgements

Appendix A

A model based on the time-domain FWH equations and spanwise strip theory is used in this work to determine the dipole noise of a realistic span model in Section VI B. To determine the sensitivity of the results to the randomisation of the time blocks, five different time block sequences (shown in Figure 24) are tested. The first sequence (TimeBlockSequence0) is simply all the blocks in numerical order. The second (TimeBlockSequence1) corresponds to the block sequence used in the results presented in Section VI B. The other remaining three sequences are randomly assigned. Figure 25 presents the comparisons of the results. It shows that the discrepancies primarily appear at low frequencies. This is expected due to the longer wavelength at lower frequencies and the relatively short signal lengths used in the prediction model making the results more sensitive to the random distribution of time data blocks. The analysis in this study is based on A-weighted spectra and the calculation of perceived noise levels. Both of these metrics are less sensitive to the uncertainties in low frequencies. The maximum deviation in the A-weighted OASPL for all five time block assignments is less than 0.24 dBA.

The original model presented in Section VI B has an original signal of 1.2 s divided into 12 time blocks with 50% overlap giving 0.2 s of data in each block. In order to show convergence, a study was performed with three different time durations. Three cases with varying total data lengths of 0.6 s, 1.2 s, and 1.8 s are considered. These cases correspond to a time block assigned to each spanwise strip of 0.1 s, 0.2 s, and 0.3 s, respectively. Figure 26 shows the noise spectra for the cases with different time durations. While there are some differences with the shortest time signal tested (0.1 s), the two results for 0.2 s and 0.3 s collapse well over the frequency range of interest. Between 0.2 s and 0.3 s, the difference in A-weighted OASPL is only 0.06 dBA. Therefore, a time duration of 0.2 seconds is selected for the time domain FWH spanwise strip theory prediction model for a realistic wing.
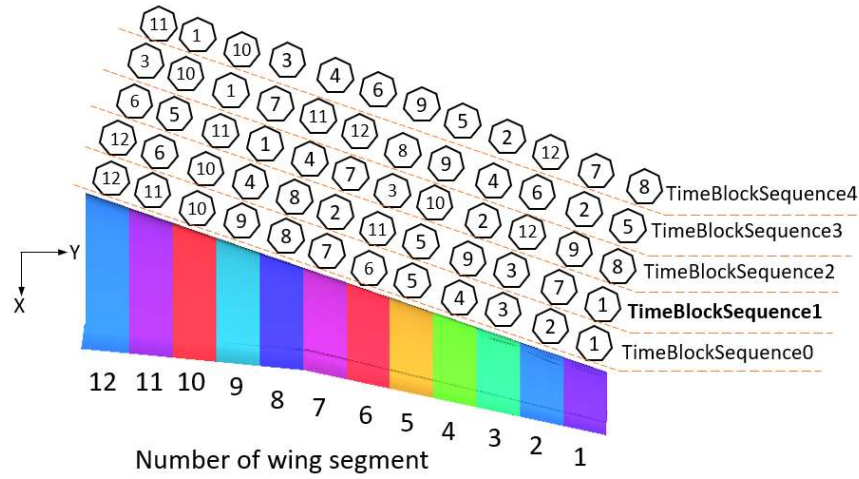

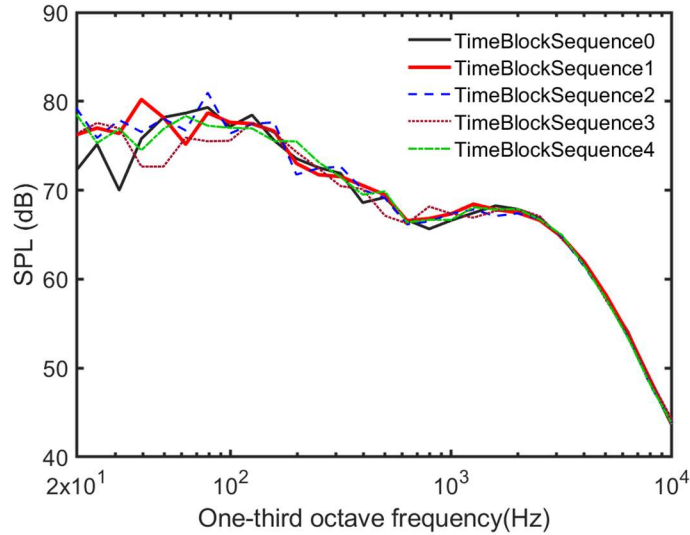**Figure 24 High-lift wing of the realistic model with 12 spanwise segments.**

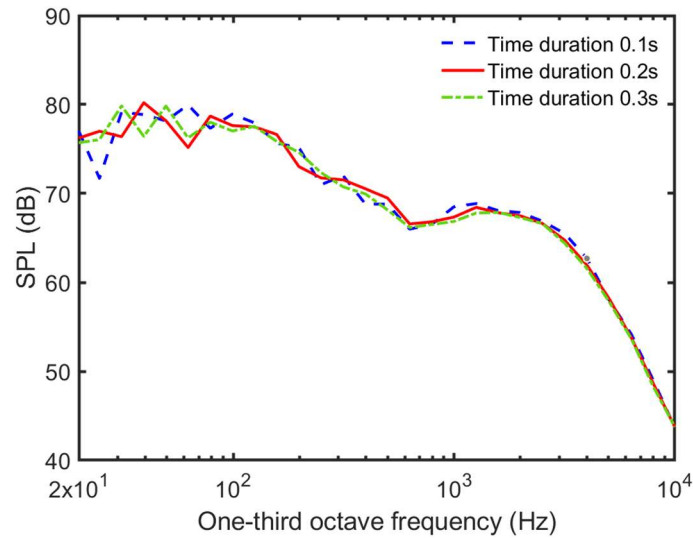**Figure 25 Comparison of noise spectra at 90° with different sequences of time blocks**

31

Figure 26 Comparison of noise spectra at 90° with different time blocks

References

[1] Morgenstern, J., Norstrud, N., Stelmack, M., and Skoch, C., "*Final report for the advanced concept studies for supersonic commercial transports entering service in the 2030 to 2035 period, N+ 3 supersonic program.*" No. PMF-01623. 2010.

[2] Brunet, M., Aubry, S., and Lafage, R. "*The clean sky programme: Environmental benefits at aircraft level,*" *15th AIAA Aviation Technology, Integration, and Operations Conference. AIAA 2015-2390.* 2015.
https://doi.org/10.2514/6.2015-2390.

[3] Ma, Y., Karpuk, S., and Elham, A., "*Conceptual design and comparative study of strut-braced wing and twin-fuselage aircraft configurations with ultra-high aspect ratio wings,*" Aerospace Science and Technology, 2022. **121**: p. 107395.
https://doi.org/10.1016/j.ast.2022.107395.

[4] Bradley, M.K. and Droney, C.K., "*Subsonic Ultra Green Aircraft Research: phase II–volume II–hybrid electric design exploration,*" NASA CR-218704, 2015: p. 378.

[5] Hosseini, S., Ali Vaziri-Zanjani, M., and Reza Ovesy, H., "*Conceptual design and analysis of an affordable truss-braced wing regional jet aircraft,*" Proceedings of the Institution of Mechanical Engineers, Part G: Journal of Aerospace Engineering, 2020: p. 0954410020923060.
https://doi.org/10.1177/0954410020923060.

[6] Torrigiani, F., Bussemaker, J., Ciampa, P.D., Fioriti, M., Tomasella, F., Aigner, B., Rajpal, D., Timmermans, H., Savelyev, A., and Charbonnier, D., "*Design of the Strut Braced Wing Aircraft in the AGILE collaborative MDO framework,*" Belo Horizonte, Brazil, 2018.

[7] Kanjere, K., Angland, D., and Zhang, X. "*A numerical study to optimise blowing flow control for flap side-edge noise reduction,*" *18th AIAA/CEAS Aeroacoustics Conference (33rd AIAA Aeroacoustics Conference), AIAA 2012-2097.* 2012.
https://doi.org/10.2514/6.2012-2097.

[8] Guo, Y. "*Prediction of flap side edge noise,*" *5th AIAA/CEAS Aeroacoustics Conference and Exhibit, AIAA-99-1804.* 1999.
https://doi.org/10.2514/6.1999-1804.

[9] Angland, D., Zhang, X., and Molin, N., "*Measurements of flow around a flap side edge with porous edge treatment,*" AIAA journal, 2009. **47**(7): p. 1660-1671.
https://doi.org/10.2514/1.39311.

[10] Hardin, J.C., "*Noise radiation from the side edges of flaps,*" AIAA Journal, 1980. **18**(5): p. 549-552.

https://doi.org/10.2514/3.7668.

[11]   Davy, R., Moens, F., and Remy, H. "*Aeroacoustic Behaviour of a 1: 11 Scale Airbus Model in the Open Anechoic Wind Tunnel CEPRA 19*," *8th AIAA/CEAS Aeroacoustics Conference & Exhibit, AIAA 2002-2412*. 2002.
https://doi.org/10.2514/6.2002-2412.

[12]   Larsson, J., Kawai, S., Bodart, J., and Bermejo-Moreno, I., "*Large eddy simulation with modeled wall-stress: recent progress and future directions*," Mechanical Engineering Reviews, 2016. **3**(1): p. 15-00418-15-00418.
https://doi.org/10.1299/mer.15-00418

[13]   Lee, S., Ayton, L., Bertagnolio, F., Moreau, S., Chong, T.P., and Joseph, P., "*Turbulent boundary layer trailing-edge noise: Theory, computation, experiment, and application*," Progress in Aerospace Sciences, 2021. **126**: p. 100737.
https://www.sciencedirect.com/science/article/pii/S0376042121000427.

[14]   Inagaki, M., Murata, O., Kondoh, T., and Abe, K., "*Numerical Prediction of Fluid-Resonant Oscillation at Low Mach Number*," AIAA Journal, 2002. **40**(9): p. 1823-1829.
https://doi.org/10.2514/2.1859.

[15]   Issa, R., "*Solution of the Implicitly Discretised Fluid Flow Equations by Operator Splitting*," Journal of Computational Physics, 1985. **62**: p. 40-65.
https://doi.org/10.1016/0021-9991(86)90099-9.

[16]   Afzal, N. and Gersten, K., "*Wake layer in a turbulent boundary layer with pressure gradient: a new approach*," Fluid Mechanics and Its Applications, 1996. **37**: p. 95-118.

[17]   Nicoud, F. and Ducros, F., "*Subgrid-scale stress modelling based on the square of the velocity gradient tensor*," Flow, turbulence and Combustion, 1999. **62**(3): p. 183-200.
https://doi.org/10.1023/A:1009995426001.

[18]   Hou, Y. and Angland, D. "*A Comparison of Wall Functions for Bluff Body Aeroacoustic Simulations.*" 22nd AIAA/CEAS Aeroacoustics Conference, AIAA 2016-2771. 2016.

[19]   Hou, Y., Angland, D., and Scotto, A. "*The ability of a weakly compressible solver to predict landing gear noise with flow-acoustic interactions*," *23rd AIAA/CEAS Aeroacoustics Conference, AIAA 2017-3008*. 2017.
https://doi.org/10.2514/6.2017-3008.

[20]   Farassat, F., "*Derivation of Formulations 1 and 1A of Farassat.*" 2007, TM-2007-214853 NASA.

[21]   Brooks, T. and Marcolini, M. "*Airfoil self noise-Effect of scale*," *8th Aeroacoustics Conference, AIAA 1983-785*. 1983.
https://doi.org/10.2514/6.1983-785.

[22]   Brooks, T.F., Pope, D.S., and Marcolini, M.A., "*Airfoil self-noise and prediction*," 1989.
https://ntrs.nasa.gov/api/citations/19890016302/downloads/19890016302.pdf.

[23]   Brooks, T., Marcolini, M., and Pope, D. "*Airfoil trailing edge flow measurements and comparison with theory, incorporating open wind tunnel corrections*," *9th aeroacoustics conference, AIAA 1984-2266*. 1984.
https://doi.org/10.2514/6.1984-2266.

[24]   Brooks, T.F. and Marcolini, M.A., "*Scaling of airfoil self-noise using measured flow parameters*," AIAA journal, 1985. **23**(2): p. 207-213.
https://doi.org/10.2514/3.8896.

[25]   Jones, B., Nagy, P., Minisci, E., and Fossati, M., "*A geometric sensitivity study for the aerodynamics of a strut-braced airframe*," Aerospace Science and Technology, 2023. **142**: p. 108638.
https://www.sciencedirect.com/science/article/pii/S1270963823005357.

[26]   Pascioni, K.A. and Cattafesta, L.N. "*Aeroacoustic measurements of leading-edge slat noise*," *22nd AIAA/CEAS aeroacoustics conference, AIAA 2016-2960*. 2016.
https://doi.org/10.2514/6.2016-2960.

[27]   Zhang, Y., Chen, H., Wang, K., and Wang, M., "*Aeroacoustic prediction of a multi-element airfoil using wall-modeled large-eddy simulation*," AIAA Journal, 2017. **55**(12): p. 4219-4233.

https://doi.org/10.2514/1.J055853.

[28]   Sanders, M.P.J., Venner, C.H., and de Santana, L.D., "*Slat noise measurements in open-jet, hard-wall and hybrid wind tunnel test sections,*" Journal of Sound and Vibration, 2023. **546**: p. 117420. https://doi.org/10.1016/j.jsv.2022.117420.

[29]   Kato, C., Iida, A., Takano, Y., Fujita, H., and Ikegawa, M. "*Numerical prediction of aerodynamic noise radiated from low Mach number turbulent wake,*" *31st aerospace sciences meeting*. 1993. https://doi.org/10.2514/6.1993-145.

[30]   Wang, M., Freund, J.B., and Lele, S.K., "*Computational prediction of flow-generated sound,*" Annu. Rev. Fluid Mech., 2006. **38**: p. 483-512. https://doi.org/10.1146/annurev.fluid.38.050304.092036.

[31]   Curle, N., "*The influence of solid boundaries upon aerodynamic sound,*" Proc. R. Soc. Lond. A, 1955. **231**(1187): p. 505-514. https://doi.org/10.1098/rspa.1955.0191.

[32]   Jiang, Y. and Filippone, A. "*Component-based model for Flap Noise Prediction,*" *25th AIAA/CEAS Aeroacoustics Conference*. 2019. https://doi.org/10.2514/6.2019-2575.

[33]   Golub, R.A. and Guo, Y.-P., "*Empirical Prediction of Aircraft Landing Gear Noise,*" 2005. https://ntrs.nasa.gov/api/citations/20050209966/downloads/20050209966.pdf.

[34]   Zhu, W.J., Shen, W.Z., Sørensen, J.N., and Leloudas, G., "*Improvement of airfoil trailing edge bluntness noise model,*" Advances in mechanical engineering, 2016. **8**(2): p. 1687814016629343.

[35]   Organization, I.C.A., "*Environmental Protection. Annex 16 to the Convention on International Civil Aviation. Volume I Aircraft Noise.*" 2008: ICAO.